Materials Science & Engineering A 849 (2022) 143484

Contents lists available at ScienceDirect

Materials Science & Engineering A

journal homepage: www.elsevier.com/locate/msea

Excellent strength and electrical conductivity achieved by optimizing the dual-phase structure in Cu–Fe wires

Fei Yang [a,b], Liming Dong [c,**], Lichu Zhou [b], Ning Zhang [d], Xuefeng Zhou [a], Xiaodan Zhang [b], Feng Fang [a,*]

[a] *Jiangsu Key Laboratory of Advanced Metallic Materials, Southeast University, Nanjing, 211189, China*
[b] *Department of Mechanical Engineering, Technical University of Denmark, Lyngby, Denmark*
[c] *School of Automotive Engineering, Changshu Institute of Technology, Changshu, 215500, China*
[d] *School of Mechanical Engineering, Southeast University, Nanjing, 211189, China*

ARTICLE INFO

Keywords:
Cu–Fe alloy
Electrical conductivity
Drawing
Dynamic recrystallization
Texture

ABSTRACT

Cu–Fe alloy wire with high strength, moderate electrical conductivity and low cost, has a promising application prospect in the electrical industry. In this study, high performance Cu80Fe20 wires were prepared by annealing and drawing at room temperature (RT). Based on the X-ray diffraction and electron microscopy characterization, the influence of microstructural parameters on the mechanical properties and electrical conductivity of the wires were analyzed. The pre-annealing at 500 °C, resulted in the nanoparticles precipitation of Cu in Fe-phase and Fe in Cu-phase, respectively. The drawing deformation greatly improved the strength of wires, while did not result in a significant reduction in the electrical conductivity. Cu nanoprecipitation promoted the refinement of the Fe-phase during deformation, which result in a nano lamellar structure of the Fe-phase with an average boundary spacing as low as 50 nm. Dynamic recovery and recrystallization of the Cu-phase were observed to occur during the drawing at RT with the <112> texture and annealing twinning. The plasticity and electrical conductivity of the Cu-phase were greatly preserved due to the drawing-induced dynamic recovery and recrystallization. Moreover, the strength of the wire was greatly enhanced by the formation of a nano-lamellar structure in the Fe-phase. Hence, the alloy wire at a strain of 3.94 had a high tensile strength of 863 MPa (125% higher than the original strain-free wire), a total elongation of 5%, and the electrical conductivity reached 47 %IACS (only 8 %IACS lower than the original strain-free wire), which shows higher cost properties than other copper alloys.

1. Introduction

Cu-based metal matrix composites (MMC) are widely used in the industries of automobiles, electronics and communication due to their high strength, the good thermal and electrical conductivity (EC) [1]. Metal transition elements with low solid solubility with copper, such as body-centered cubic (Nb, Cr, Fe) or face-centered cubic (Ag, Al, Ni) elements, are usually selected as the second phase in Cu-based MMC. Among them, Cu–Fe alloy arising from its low raw material cost and relatively high strength, can be applicated as a candidate for electromagnetic shielding conductor materials. Previous research has shown that [2], there is a very high positive enthalpy between liquid Cu and Fe phases. During the solidification process, γ-Fe first precipitates, then a peritectic reaction occurs, and finally, a mixture composed of Fe-rich and Cu-rich phases is formed. Combined with the action of the high solubility of Fe in Cu at high temperature and the slow diffusion speed of Fe at low temperature, a small amount of Fe inevitably remains in the Cu matrix, which is unfavorable to the EC of Cu phase [3]. For example, the EC will drop by approximately 50% when the iron content in the copper matrix reaches 0.05 wt% [4]. Therefore, promoting the precipitation of Fe from Cu and improving its EC without sacrificing the strength of Cu–Fe alloy has become a design strategy. For instance, the FeSi phase precipitated after 0.4 (wt%) Si element was added into Cu–10%Fe [5], and the alloy can obtain strength of 521 MPa and electrical conductivity of 68.02 %IACS after cold rolling.

At present, Cu–Fe alloys with a high iron content (greater than 5 wt%) are mainly prepared by spray deposition, powder metallurgy, and combustion synthesis. The uneven distribution of Fe phase in the Cu

---

* Corresponding author. School of Materials Science and Engineering, Southeast University, Jiangning District, Nanjing, 211189, China.
** Corresponding author.
E-mail addresses: donglm@cslg.edu.cn (L. Dong), fangfeng@seu.edu.cn (F. Fang).

https://doi.org/10.1016/j.msea.2022.143484
Received 21 April 2022; Received in revised form 15 June 2022; Accepted 16 June 2022

matrix has been effectively solved. However, the disadvantages of these technical processes are also obvious, such as large equipment investment, small ingot specifications, low density, low production efficiency, and high production cost. To regulate the microstructure and properties of Cu–Fe billets, Stepanov [6] cold rolled Cu-14% Fe, which led to a significantly improved strength but seriously reduced plasticity simultaneously. Wang et al. [7] prepared Cu-10% Fe alloy plates by double melt mixed casting and cold rolling. After cold deformation, the coarse dendrite structure is broken, and the Fe phase is fiberized along the rolling direction. The strength of alloy increases from the initial 340 MPa–543 MPa, at an expense of a catastrophic decreases of the EC from 56.7 %IACS to 13.5 %IACS. Similarly, after cold rolling of Cu-6.5Fe-0.3 Mg [8], the tensile strength and electrical conductivity reached 558 MPa and 35.1 %IACS, respectively. After suffering cold rolling and annealing [9], the Cu10Fe0.5Ag alloy obtains a hardness of 180HV and an electrical conductivity of 35%IACS. Compared with rolling, cold drawing can greatly improve the strength but reduce damage to the EC and has become the main forming method for preparing high-performance Cu–Fe alloy [10]. For example, Wang [4] cold drawn Cu-15% Fe prepared by powder metallurgy and found that after suffering drawing strain of 6, the tensile strength was increased to 1200 MPa, and the EC was maintained at 47.6 %IACS. In terms of strength, Chatterjee [11] investigated the strengthening mechanisms for as-cast Cu–Fe alloy, and found that the change in strength is dominated by the morphology of Fe phase [12,13] but less affected by the change in dislocation configuration and grain size [14]. Spitzig [15] concluded that the density of dislocation will not continue to increase with the increase of drawing deformation processing, and the relationship between the strength and layer spacing of Nb filaments in Cu–Nb wires conforms to the Hall-Petch relation, and the former is considered to be equally applicable to the Cu–Fe alloy [6,7]. For EC, almost all strengthening factors contribute to lattice distortion, aggravate electron scattering and reduce the electron transmission efficiency [16]. Therefore, in various metals, EC and strength are contradictory. Achieving a combination of high strength and good EC in Cu–Fe materials has become a major challenge [17]. Apart from that, current research on Cu–Fe alloy mainly focuses on the preparation process. The characterization and analysis of microstructure during cold drawing are not profound, especially the evolution of the second phase and texture, as well as the effect of microstructural parameters on the both the mechanical performance and electrical conductivity [18].

In this work, the Cu-20% Fe ingot was thermally deformed, and then the insoluble coarse iron dendrites in the copper matrix were broken and scattered so that the fine iron particles are uniformly distributed. Annealing was taken to promote the precipitation of Fe in the copper matrix to improve the EC of copper matrix. Finally, Cu-20 wt% Fe alloy wire with high strength, high toughness and high EC were prepared by cold drawing. The main purposes of this study are: (1) to take advantage of microstructure characterization to clarify the evolution law for the copper phase and iron phase during the drawing process; (2) to calculate the formula revealing the main influence mechanism of the drawing strain on the strength and EC.

2. Material and methods

Cu and Fe blocks with purities higher than 99.9% were selected as raw materials, and an ingot with dimensions of Φ50×250 mm^3 was prepared by vacuum induction melting. The nominal composition of the alloy ingot is Cu80Fe20 (wt%). The actual element content is measured by direct reading spectrometer (MAXx LMF15, Spectro, Germany), which is Fe 20.03 wt%, Cu 79.89 wt%, and the remaining impurity element content does not exceed 0.08 wt%. The ingot was heated to 1000 °C in a pit-type resistance furnace and held for 30 min. The ingot was slowly formed into a round bar by rotary forging at room temperature. When the temperature of the bar is lower than 800 °C, it is put into the furnace and reheated to 1000 °C for 10 min, and then the rotary forging is continued at room temperature, and finally a bar with a diameter of 14 mm was obtained, the total forging strain (ε) reaches 2.55. The calculation formula of drawing strain is $\varepsilon = 2\ln(d_0/d_i)$, where d_0 and d_i correspond to the initial diameter and diameter of the wire after the i passes drawing, respectively. After annealing at 500 °C for 1 h, the alloy rod was machined to a diameter of 12 mm. Alloy wires with different strains were obtained through the multi-pass drawing at room temperature. The wires with diameter of 8.8 mm, 4.28 mm and 1.68 mm were selected for microstructure characterization, the corresponding drawn strain are 0.62, 2.06 and 3.94, respectively. The microstructure of the alloy wires was characterized by optical microscopy and field-emission scanning electron microscopy (Fei-Sirion). EBSD was also used to analyze the microstructure and texture for the alloy wires at 20 kV and with a scanning step of 0.1–0.12 μm. After mechanical grinding and polishing, the samples were surface treated by argon ion polishing, and the HKL channel 5 software was used for the visualization of EBSD data. XRD (Smartlab 3) was used to detect the changes in lattice constant of both Cu-phase and Fe-phase. TEM samples were prepared by the GATAN PIPS 691 ion milling system and observed by Talos F200X and FEI Tecnai G2. The schematic diagram of tensile specimen geometry is shown in Fig. 1. The tensile tests of wires were carried out at room temperature with a strain rate of 5×10^{-3} s^{-1}. The complete stress-strain curve was obtained by using a uniaxial tensile testing machine (CMT5105) equipped with an extensometer. Each group of samples was tested three times. A HIOKI-RM3548 ohmmeter was used to measure the electrical resistivity of alloy wires, and the measurement accuracy was within 0.1 μΩ. To ensure the accuracy of the test, the wire after each drawing pass was tested after cooling the sample down to room temperature. Each wire was measured in three sections to obtain the average value. The International Annealed Copper Standard (%IACS) was utilized to calculate the EC of alloy wires, and the calculation by $W(\%IACS) = \frac{L}{R\cdot S\times5.8\times10^{7}}\times 100\%$, where R is the resistivity of the sample, L stands for distance between the measurement points, and S represents the cross-sectional area of the alloy wires.

3. Results

3.1. Pre-treatment microstructure

Fig. 2 shows the perpendicular microstructure of Cu–Fe alloy rods after different pre-treatments. As shown in Fig. 2a, coarse primary Fe dendrites and some Fe particles are observed in the ingot, and the growth of dendrites has a certain directionality (as shown by the arrow). The subsequent hot forging deformation destroys the original oriented dendrites with severe local deformation (Fig. 2b). After annealing at 500 °C, the Fe particles (the darker one in Fig. 2c) are more uniformly dispersed in the Cu matrix, and the average size of the particle is 3.2 ± 1.1 μm (upper right corner in Fig. 2c). Based on the XRD pattern in Fig. 2d, the Cu–Fe alloy is only composed of Cu and Fe phases in the 500°C-annealed samples, and also in the drawn wires.

After the 500°C-annealing, the Fe and Cu phase exhibit random crystal orientation, as shown in the IPF figure (Fig. 3a). The thick black

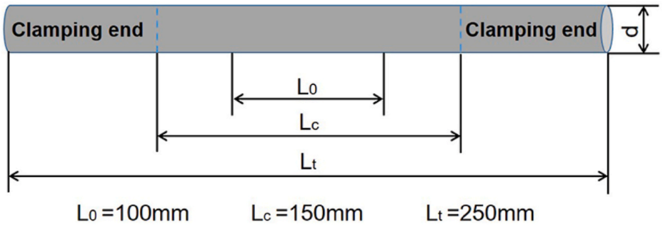

Fig. 1. Schematic diagram of the tensile specimen geometry. The ‘d’, ‘L_0’, ‘L_c’ and ‘L_t’ refers to diameter, original gauge length, free length and total length, respectively.

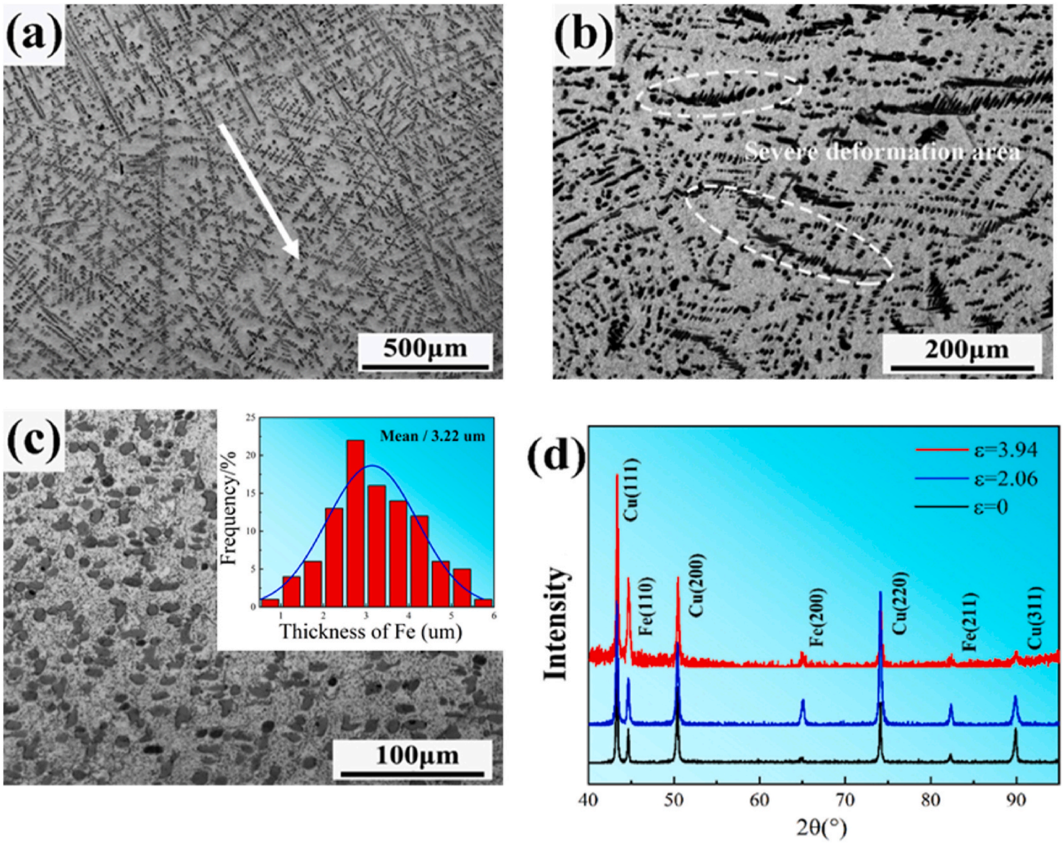

Fig. 2. Microstructure and phase identification of Cu–20%Fe (a) ingot, (b) hot forged, (c) annealed and size distribution of Fe, (d) the XRD pattern.

line shows the high-angle grain boundary (HAGB, >15°), the thin green line shows the low-angle grain boundary (LAGB, 2–15°). In the Cu matrix, a large number of annealing Σ3-twin boundaries (red lines in blue area in Fig. 3b) are also identified. Fig. 3c shows the nano-Fe precipitates in the Cu matrix, and based on the HRTEM analysis in Fig. 3(d-e), the nanoparticle is identified as bcc-Fe and shares a clear crystal orientation relationship with Cu matrix, that $(1\bar{1}1)_{Cu}//(\bar{1}10)_{Fe}$.

In the Fe-phase, Fig. 3f shows that the high-density copper-rich particles with an average size of 65 nm are evenly distributed. The select area electron diffraction (SAED) confirms that the Fe-phase and Cu-rich particles share a Kurdjumov-Sachs (KS) orientation relationship, $(1\bar{1}1)_{Cu}//(\bar{1}10)_{Fe}$ and $<011>_{Cu}//<111>_{Fe}$ (Fig. 3g). A large number of dislocations were observed in Fe-phase (Fig. 3h). These dislocations are formed during the hot forging and inherited. It can be speculated that the precipitated Cu-rich particles also suppressed the dislocation recovery in Fe-phase during the 500°C-annealing. Unlike the high-density independent dislocations in Fe-phase, there are relatively few dislocations in the Cu-phase, it is because 500 °C is high enough for the recrystallization of Cu matrix.

3.2. *Microstructure of cold drawn alloy wires*

Fig. 4 shows the phase distribution and orientation of the wires at different drawing strains. After low drawing strain deformation ($\epsilon = 0.62$), the Fe phase is slightly elongated, and shows a <110> texture. However, the elongated structure and preferred orientation of Cu phase are not obvious (Fig. 4a). As ϵ increased to 2.06 (Fig. 4b), the Fe phase exhibits a serious fiber structure which is parallel to the drawing direction, while the Cu grains just show a slight refinement. When drawing strain reaches to $\epsilon = 3.94$, the Fe fiber is further refined, but the fragmentation is also evident (Fig. 4c). At this time, copper shows strong <111> texture.

The average size of copper grains in transverse and longitudinal directions are measured by the intercept method, and the statistic results are shown in Fig. 4d. Although the alloy wires were seriously drawn from Φ12 mm to Φ1.6 mm, the length and thickness of Cu grains were only decreased by 50%. The aspect ratio of copper grains was measured to maintain between 1.6 and 2.5, which is much lower than that of pure drawn copper wires (with a maximum of 4.6) [19], indicating that the Cu phase did not suffer from severe elongation and refinement deformation. It is noticed that, orientation of Cu phase changes a lot during the drawing process, as shown in Fig. 4e. The volume fraction of <111> texture increases monotonically with the drawing deformation processes, the <112> texture first increases and then decreases, and achieves the peak value when the drawn strain reaches around 2.06.

Fig. 5 shows the microstructure evolution of copper particles in the iron phase during drawing. When $\varepsilon = 0.62$, a slight deformation occurs along the drawing direction, and the shape changes from spherical to ellipsoidal. At $\varepsilon = 2.06$, the copper particles are obviously elongated to form a flat lenticular structure. At a strain of 3.94, a fibrous structure intersecting the Fe matrix sheet is formed. The variation of the thickness of Cu particles is statistically in Fig. 5d. From spherical particles to fiber structure, the size of rich Cu phase is also refined from 70 nm to 10 nm, indicating that Cu particles in Fe phase are seriously elongated by drawing deformation. The thickness of Fe fiber at drawn strain of 3.94 is displayed in Fig. 5e. It can be found that due to the existence of Cu fibers, the thickness of Fe fiber in Cu–Fe wires is only 1/4 of that of pure Fe wire at the same drawing strain [20], even lower than the refining limit of pure Fe fiber, it is about 80 nm at the drawn strain of 10.35.

Fig. 6 shows the bright field TEM images of the copper phase in drawn wires. When the strain is 0.62, the drawing leads to a large number of dislocations. The nano-iron particles in the copper matrix pin the dislocation glide, leading to a large number of dislocations piled up around the second phase. When the strain increases to 2.06, dislocation

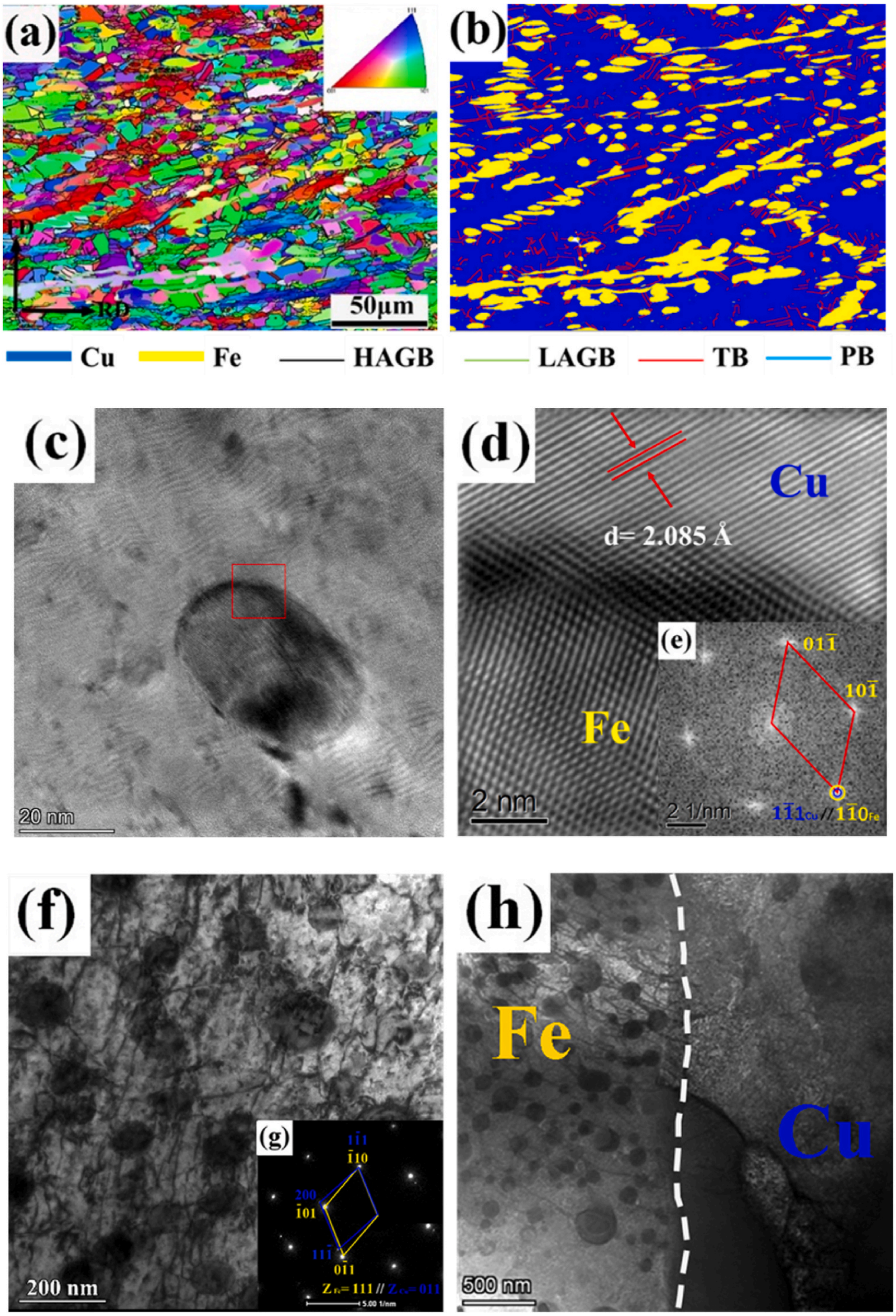

Fig. 3. Microstructure of the annealed Cu–20%Fe alloy (a) Inverse pole figures, (b) EBSD phase distribution diagrams, (c) HRTEM of the Cu phase, (d) solid red frame in c, (e) FFT (Fast Fourier Transform) of d, (f) bright field image of the Fe phase, (g) select area electron diffraction, (h) dislocation morphology in two phases. (For interpretation of the references to colour in this figure legend, the reader is referred to the Web version of this article.)

cells and dislocation substructures are formed along the drawing direction. After severe drawing deformation at ε = 3.94, significant elongation deformation occurs in the drawing direction of the copper grains. Unlike the severe elongation deformation of the Fe phase, the Cu phase was not refined severely. The average width of the transverse grain is measured to be 200 ± 40 nm, which is much bigger than that of the Fe fiber (approximately 50 ± 10 nm), as shown by the white dotted line in Fig. 6c. At the same time, it is observed that a large number of nano iron particles continue to exist in the copper matrix in the form of ellipsoids (shown by the yellow solid line), indicating that these iron particles are less affected by the drawing deformation.

3.3. Mechanical and electrical properties

The tensile properties of Cu–Fe alloy wires corresponding to different drawing strains are shown in Fig. 7a, and the tensile properties are listed in Table 1. The pretreated alloy is provided with an ultimate tensile strength (UTS) of 380 MPa and total elongation (TE) of 33.5%. As the

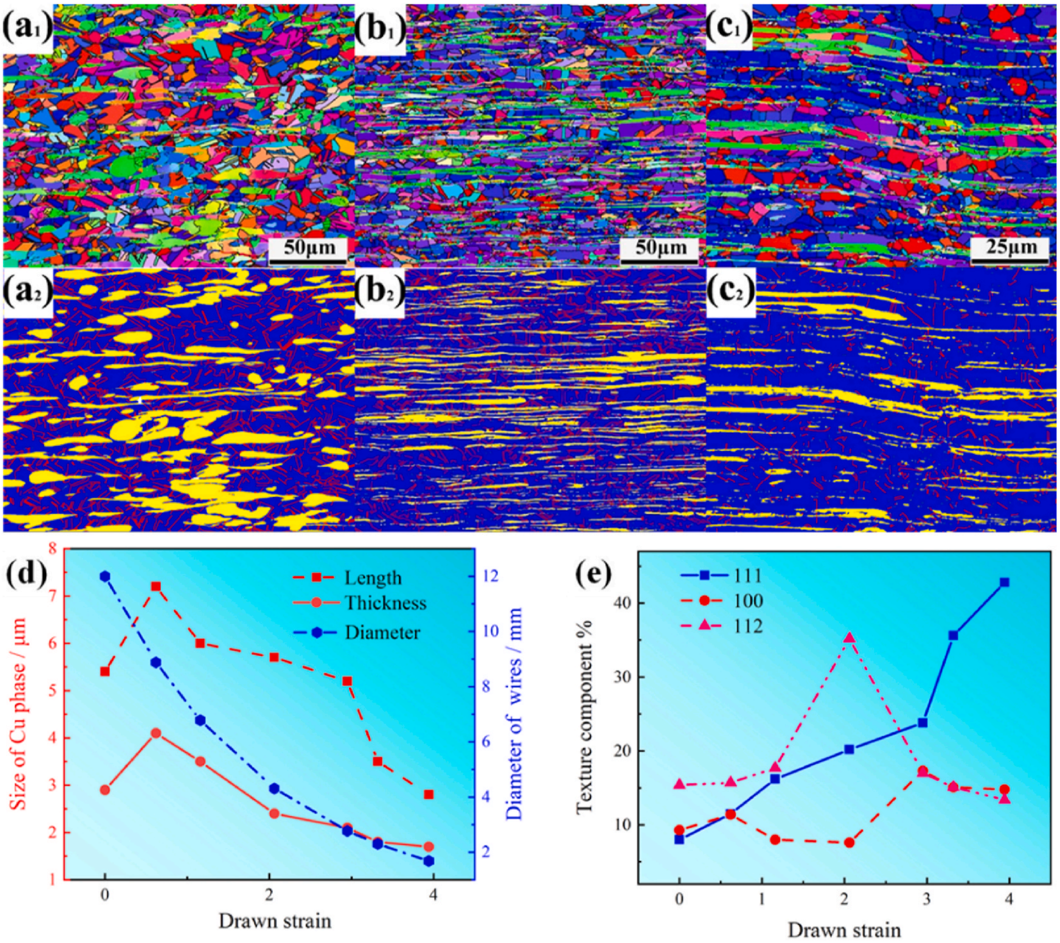

Fig. 4. Microstructure and texture for the Cu–20%Fe alloy wires (a_1, a_2) $\varepsilon = 0.62$, (b_1, b_2) $\varepsilon = 2.06$, (c_1, c_2) $\varepsilon = 3.94$, (d) grain size of Cu phase and diameter of Cu–Fe wires versus drawn strain, (e) the texture component of Cu matrix.

drawn strain increases, the tensile strength of the Cu–Fe alloy wires continues to increase at the cost of reduced plasticity. When the drawing strain is 3.94, the UTS increases to 863 MPa, and the TE decreases to 5%. It should be noted that, the strength and plasticity are better than that of pure copper wire (UTS <450 MPa, FE < 2%) at the same strain [19], and higher than that of Cu–Fe alloy plate obtained by cold rolling process [6,7,10]. Fig. 7b shows the EC evolution of Cu–Fe alloy wires corresponding to the drawing strain. The change in EC can be divided into four stages: 1st $\varepsilon < 0.4$, the EC decreases significantly from 54.7 %IACS to 50.96 %IACS; 2nd $0.4 < \varepsilon < 1.16$, the EC increases; 3rd $1.16 < \varepsilon < 1.85$, the EC is nearly stability to approximately 54 %IACS; 4th $\varepsilon > 1.85$, the EC decreases monotonically. Generally, in the process of plastic deformation, the dislocation density and interface density will increase by orders of magnitude in the alloy, thus increasing the dislocation scattering resistivity and interface scattering resistivity [4].

3.4. *Comprehensive performance comparison*

For copper alloys, the tensile strength and EC are the most important properties. The distribution of EC and UTS of various copper alloys is displayed in Fig. 8a [4,7,13,19,21–32]. It can be seen that copper and Cu–Ag alloys achieve better EC, while the UTS of Cu–Nb alloy is the highest. However, for industrial applications, the alloying cost should be taken into consideration. Divide the properties by the alloy unit price (¥/kg), and the concept of cost properties is proposed, which is expressed as UTS/cost and EC/cost respectively, as shown in Fig. 8b. Pure copper occupies the lower right corner and is widely used in non-load-bearing electrical fields, such as generator coils, vacuum tubes, semiconductor wires, etc. The Cu–Nb and Cu–Ag occupy the lower left position, and show the lowest cost properties, resulting in a limited application of these materials. Among the existing alloy systems, Cu–Fe exhibits higher strength, moderate EC and lowest cost. By adjusting the microstructure through thermos-mechanical, the Cu–Fe alloys could be provided with a wide distribution of comprehensive properties, which occupies the center-upper part of the picture. The balanced comprehensive properties promise the application of Cu–Fe alloys in overhead transmission lines, distribution lines, and construction lines. In this work, a UTS of 863 MPa and an EC of 50 %IACS is achieved by cold drawing. Compared to the annealed sample, the strength is more than doubled while the EC is reduced by only less than 10%.

4. Discussion

4.1. *Dynamic recovery and recrystallization (DRR) of Cu matrix*

Generally, <111> and <100> fiber textures are formed in the single-phase copper after the drawing deformation [19]. However, as shown in Fig. 4, there are still a considerable number of copper grains with random orientations. The orientation distribution function (ODF) of $\Phi_2 = 45^\circ$ is employed to shows the detailed texture evolution of the Cu-phase during the drawing, and the Miller indices corresponding to the Euler angle are shown in Fig. 9. The annealed sample shows a random texture which may be caused by the hot-forging. At $\varepsilon = 0.62$, a <111> texture forms in the Cu phase. At $\varepsilon = 2.06$, the <111> texture transforms to the <112> texture, and the <112> texture shows the highest intensity. When the drawing strain is further increased to 3.94,

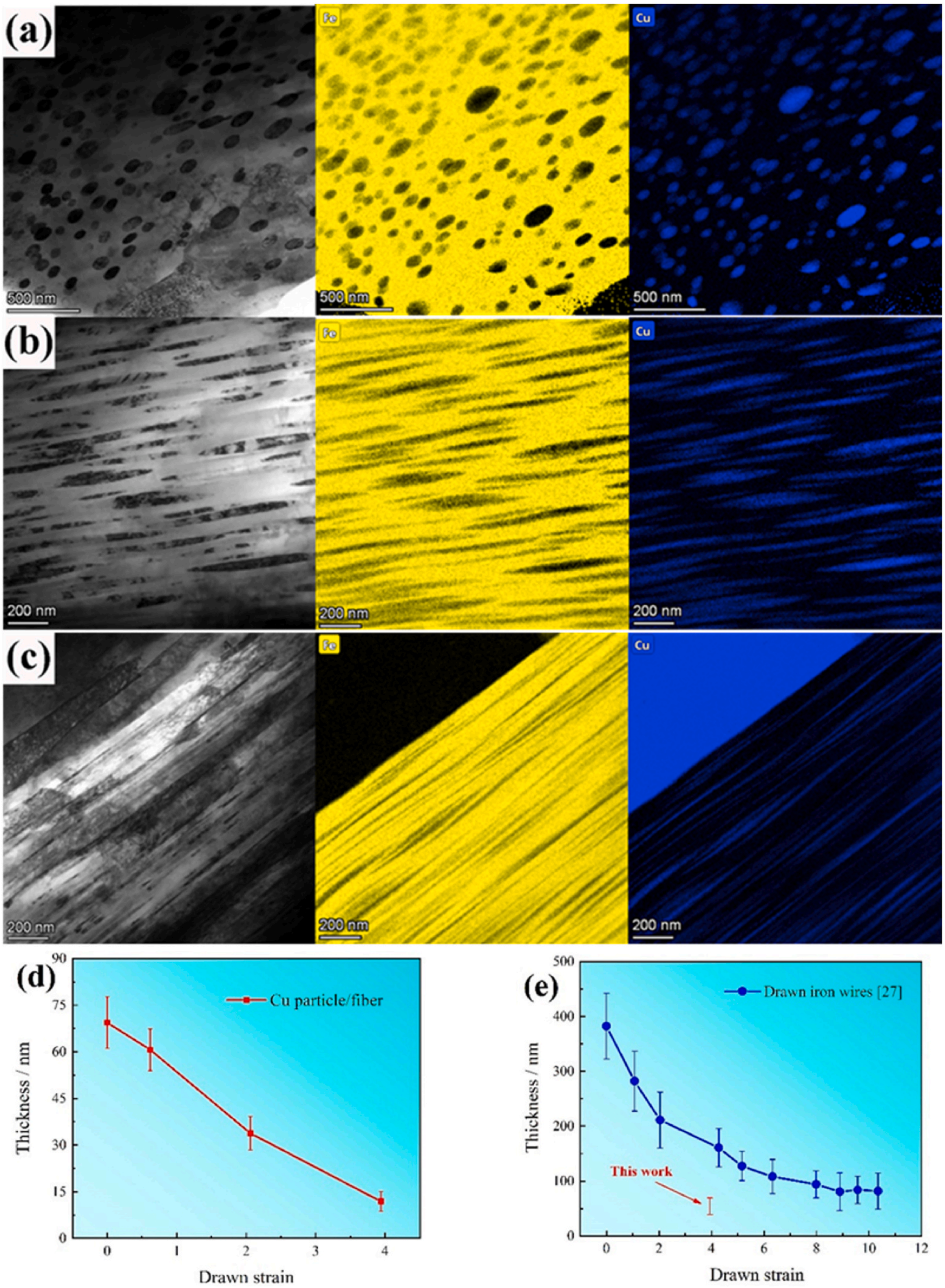

Fig. 5. Bright field TEM and EDS for copper particles in Fe phase.(a) $\varepsilon = 0.62$, (b) $\varepsilon = 2.06$, (c) $\varepsilon = 3.94$, (d) the thickness evolution of copper particles/fibers, (e) the thickness evolution of iron fibers.

the Cu phase has a dominant <111> texture. According to the report, the Schmidt factors of the <001> orientation is in the ranges of 0.42–0.46, which higher than that of <111> orientation, about 0.3–0.34 [19]. A smaller Schmidt factor represents a larger yield strength required for deformation. Therefore, the yield strength of grains with <111> orientation is greater than that of grains with <001> orientation. Hou [33] studied the contribution of texture to strength in drawn aluminum wire, and the strength increased by only 18 MPa when the volume fraction of <111> texture reaches 76%. Considering the highest volume fraction of <111> texture in drawn Cu–Fe alloy wire is only about 40%, the contribution of texture to strength is almost negligible.

According to Baudin's research [34] on the annealing structure of cold-drawn copper wire, the <112> texture can be considered as a result of annealing. Due to the initial recrystallization temperature of deformed copper is low, about 150 °C in nano-laminated copper [35], high isolation thermal stress caused by drawing strain of the Cu–20%Fe alloy results in continuous DRR of the copper phase. Although hot forging and annealing are carried out before drawing, a small amount of Fe element remained in the copper matrix, may inevitably increase the critical temperature required for DRR of the Cu matrix. Fig. 10 shows a typical annealing twin in Cu-phase observed in the wire at $\varepsilon = 2.06$ up to 20 nm thick, which is wider than the nanometer thickness of deformation twins in copper alloys. It confirms that the DRR of Cu-phase occurs during the drawing, together with the EBSD results.

Fig. 11 shows the boundary distribution and kernel average misorientation (KAM) of the cold drawn wires. It can be seen that in the

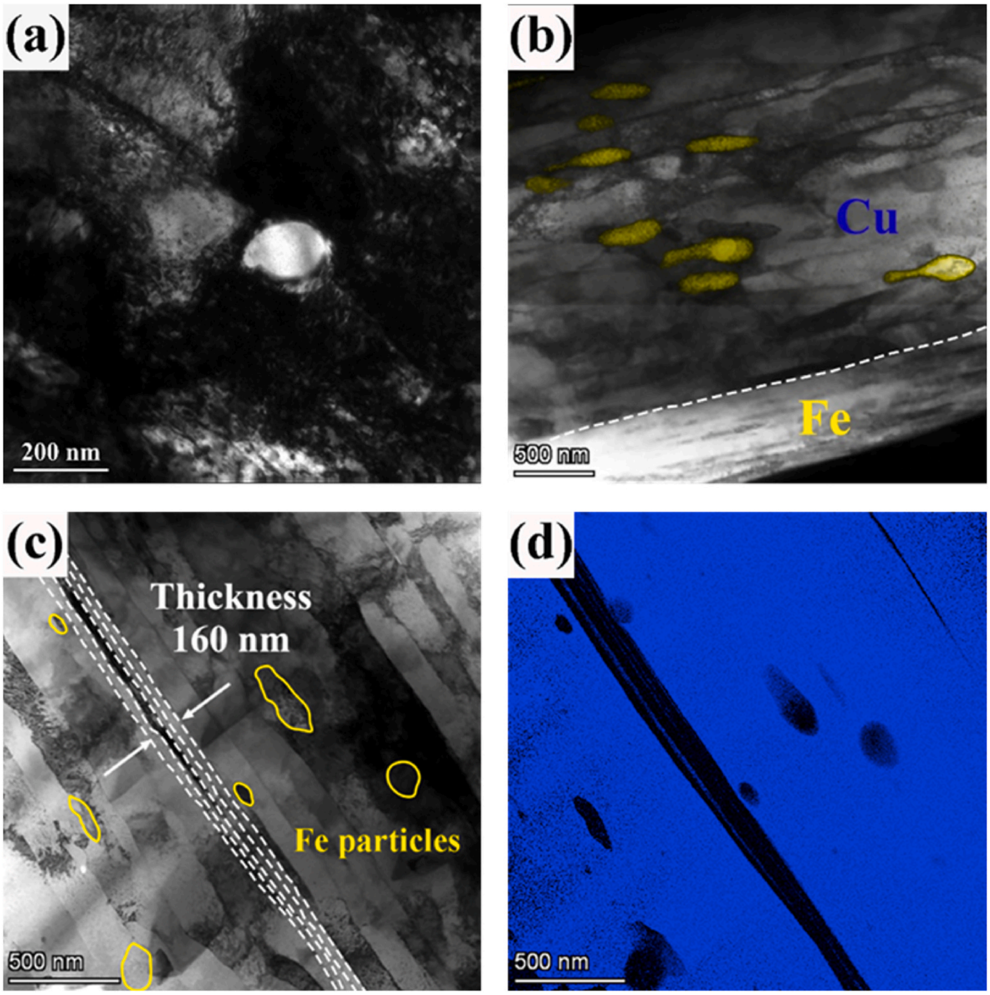

Fig. 6. Bright field TEM for the Cu matrix in wires at strain of (a) ε = 0.62 (b) ε = 2.06, (c) ε = 3.94, (d) element mapping of Cu in (c).

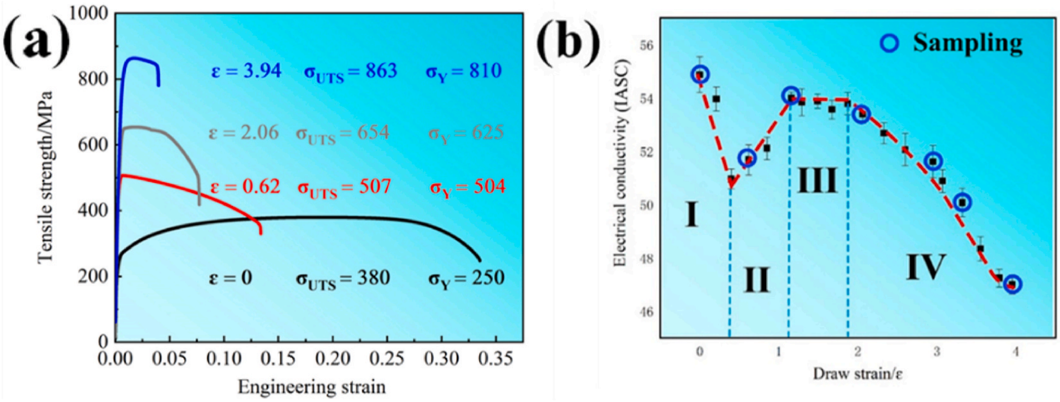

Fig. 7. Cold-drawn Cu–Fe wires (a) Engineering stress-strain curve, (b) electrical conductivity versus drawing strain.

annealed samples (Fig. 11a$_1$), the LAGB is mainly concentrated in the Cu phase. Meanwhile, after drawing deformation the LAGB in Cu phase decreased obviously but generated in Fe phase (Fig. 11b$_1$-d$_1$). The KAM was utilized to characterize the degree of plastic deformation of the two phases. In the annealed wires, the misorientation in Cu is higher than that in Fe phase. Drawing deformation results in a decrease of the misorientation in Cu and an increase in Fe phase. Interestingly, in the wires with large strain (Fig. 11 d$_3$), the misorientation in the copper phase is more concentrated. According to the grain boundary distribution, the serious mismatch area in the Cu phase is mainly focused on the grain LAGBs (shown by the orange arrow). Therefore, it can be inferred that in the drawing process, the isolation heat produced by the two-phase material is higher than that of the single-phase copper wire, and the DRR is more significant. Under the joint effect of work hardening and DRR, the dislocations in the copper grain continue to proliferate and recover. For the high-density dislocation region, dislocations accumulate and annihilate at the dislocation cell wall, the cell wall absorbs dislocations, and dislocations gradually change into sub-grain

Table 1

Tensile properties of cold drawn wires.

D/mm	Strain	UTS/MPa	Elongation %
12.1	0	379.6 ± 4.5	33.5 ± 1.3
8.88	0.62	506.7 ± 3.4	13.4 ± 1.2
6.78	1.16	566.1 ± 1.4	8.3 ± 0.8
4.31	2.06	654.1 ± 5.6	7.7 ± 0.9
2.77	2.95	756.3 ± 6.3	7.1 ± 0.9
2.3	3.32	802.2 ± 5.2	5.8 ± 0.5
1.68	3.94	863.4 ± 4.7	4.0 ± 0.5

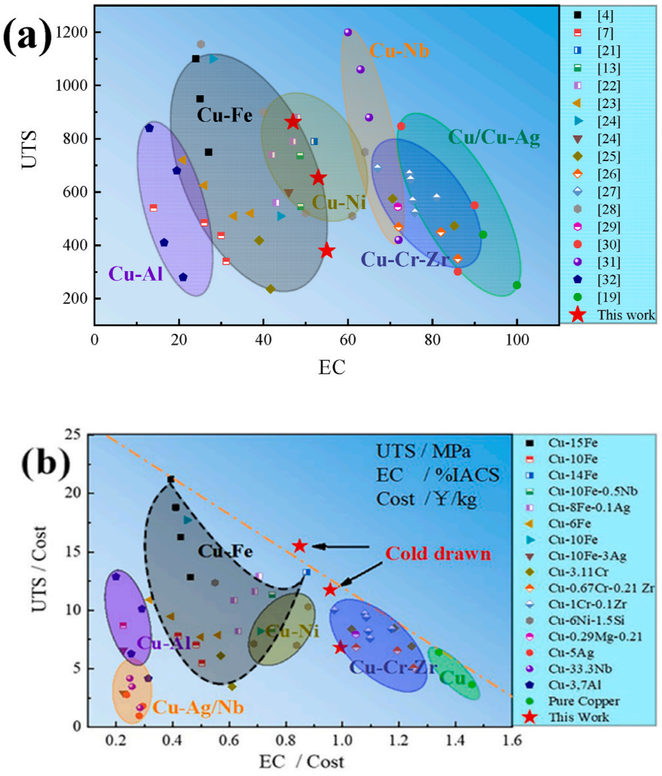

Fig. 8. (a) EC and ultimate tensile strength, (b) properties/cost for different copper.

boundaries with large misorientation. The larger the drawing strain is, the more the newly formed grain boundaries are.

4.2. Mechanical properties

Stepanov [6] studied the mechanical properties of Cu–Nb and Cu–Fe materials and concluded that the tensile strength and the average spacing of the second lamella conform to the Hall-Patch relationship, that is:

$$\sigma_C = \sigma_0 + k\lambda^{-0.5} \tag{1}$$

where σ_0 is the stress required for dislocation slip in the copper phase and iron phase, λ represents the average spacing between Fe particles. However, this conclusion is difficult to apply to present experiment, for the following two reasons:

1) Only the influence of the second phase is considered, while the contribution of dislocations and Fe solid solution to strength is ignored. With the increase of drawing strain, the dislocation morphology gradually changes from a single dislocation to dislocation entanglement, dislocation cell and dislocation boundaries (Fig. 6). The higher the dislocation density, the more strength contribution from work hardening. Because the strengthening effect of dislocations in FCC Cu with the BCC Fe is different, the dislocation strengthening needs to be discussed separately;

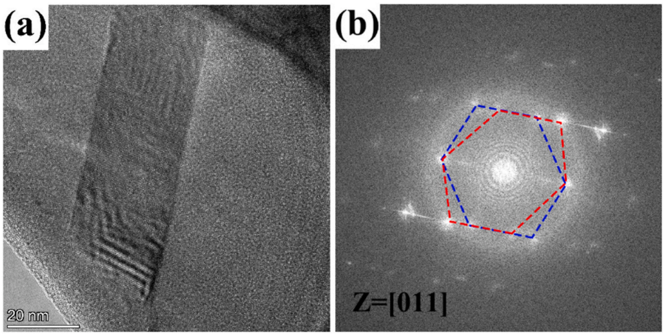

Fig. 10. High resolution of an annealing twinning at ε = 2.04.(a) morphology; (b) the FFT pattern.

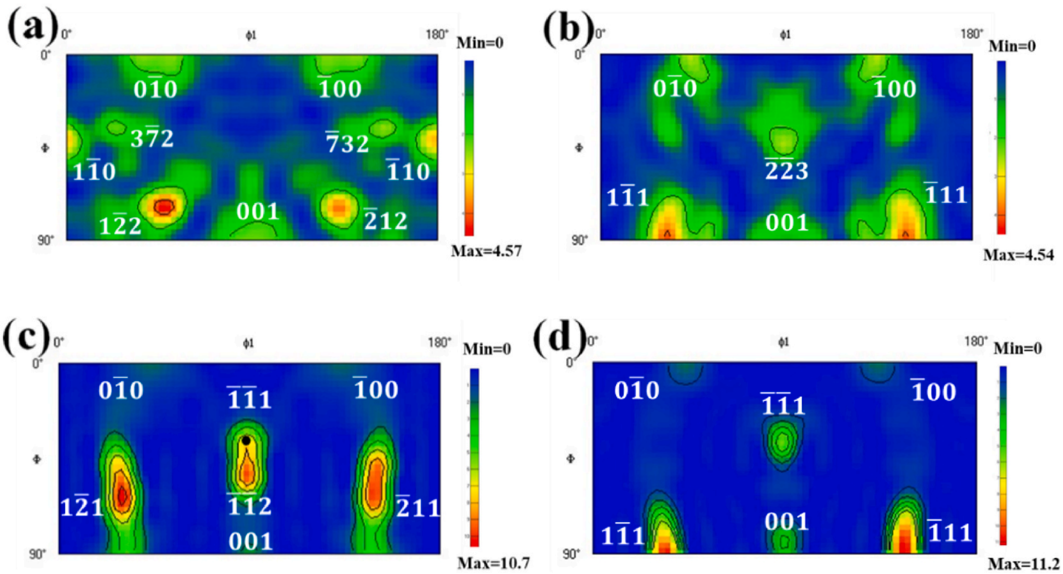

Fig. 9. ODF at $\Phi_2 = 45^\circ$ of (a) annealed, (b) ε = 0.62, (c) ε = 2.06, (d) ε = 3.94.

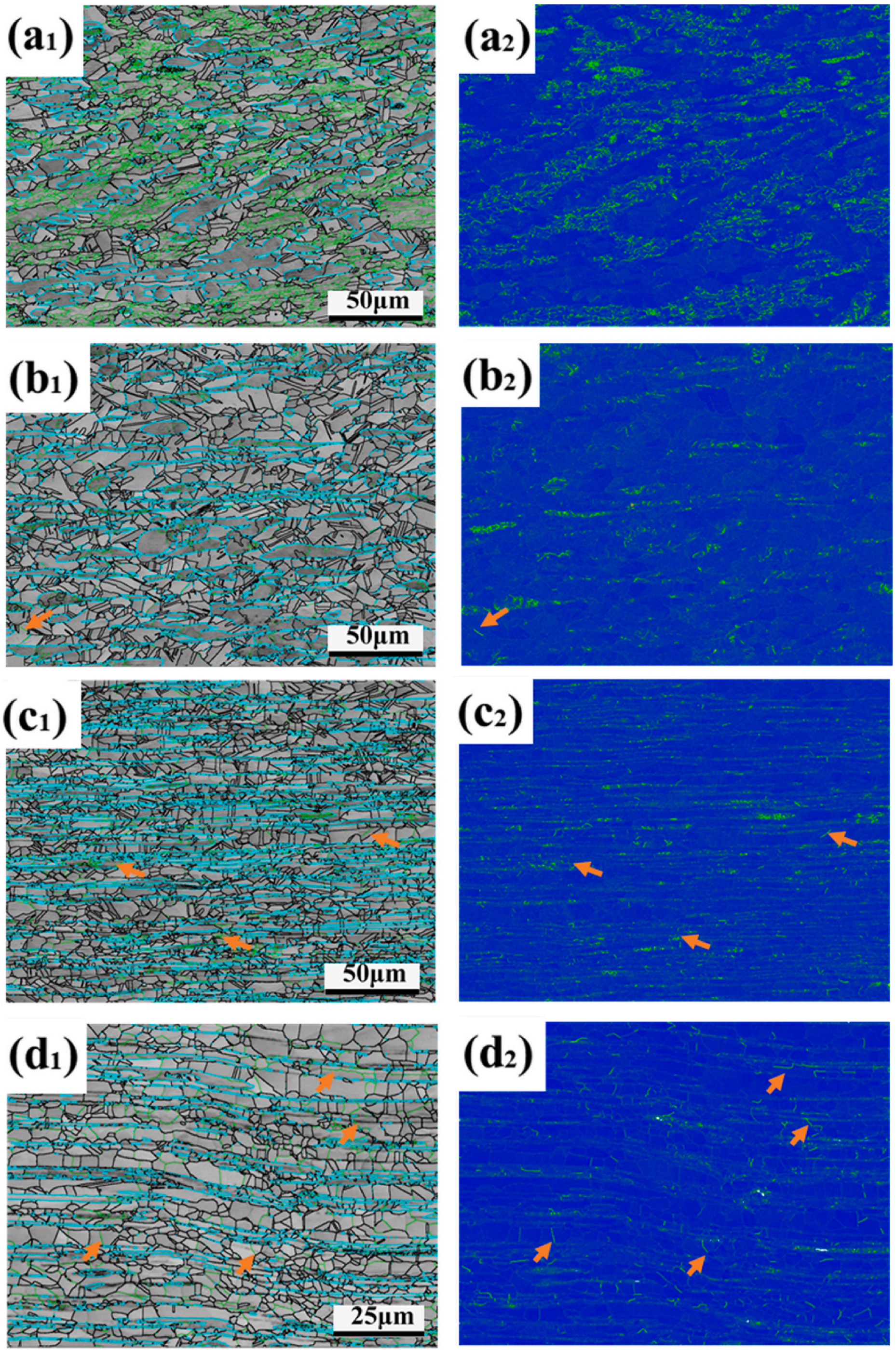

Fig. 11. Boundary distribution and KAM of (a) annealed, (b) ε = 0.62, (c) ε = 2.06, (d) ε = 3.94.

2) Through the drawing deformation, the fiber structure of copper and iron lamella intersection is formed in the iron phase, while the density of nano iron particles in the copper phase is low and the degree of deformation is small. Considering the larger proportion of the copper phase in the structure, it is one-sided to measure the lamellar spacing in the Fe phase only by TEM. Therefore, the above formula is not applicable to the drawn Cu-20% Fe material studied in this work.

Different from pure metal deformation, the effects on the strength arising from the solid solution elements in the alloy should also be considered in Cu–Fe alloys. The increase in the yield strength caused by the solid solution can be expressed as [17]:

$$\Delta\sigma_{solid\ solution} = G\left(|\delta| + \frac{1}{20}\right)|\eta|^{\frac{3}{2}}\sqrt{\frac{x_\alpha}{3}} \tag{2}$$

$$\eta = \frac{d_{lnG}}{d_x} = \frac{1}{G}\cdot\frac{d_G}{d_x} \tag{3}$$

where δ is the factor of lattice change, η is the shear modulus change factor caused by alloying, and x is the atomic percentage of the solute atoms in the matrix. Heterogeneous atomic solutes in Cu matrix may lead to lattice distortion and hinder the dislocation glide, thus improving the yield stress of the alloy. According to the HRTEM (Fig. 3d) result, the deviation of $(111)_{Cu}$ crystal plane spacing between the measured value and the standard value is about ±0.001 Å. Therefore, the solid solution strengthening could be negligible. In the Cu–10%Fe alloy, Wang [17] calculated that the strengthening of the Cu matrix by the solid solution of Fe element is only about 1.2 MPa. Then, the strength of the drawn Cu–Fe alloy wires is mainly contributed by the dislocation strengthening, the boundary strengthening and second phase hardening.

Chatterjee [11] reports that the values for the strength enhancement due to grain refinement and dislocation of Cu and Fe can be calculated through the Hall-Patch formula and the dislocation strengthening model, respectively. Then the contribution of strengthening factors can be comprehensively analyzed by using the mixing law. The main calculation formula is expressed as follows:

$$\sigma_y = 0.22\sigma_{yFe} + 0.78\sigma_{yCu} \tag{4}$$

where 0.22 and 0.78 represent the volume fraction of Fe and Cu, respectively. σ_{yCu} is the contribution of grain refinement and dislocation to strength, and the calculation formula is expressed as follows [36]:

$$\sigma_{yCu} = \sigma_{GB} + \sigma_{DIS} \tag{5}$$

$$\sigma_{GB} = 25 + 120d_{Cu}^{-0.5} \tag{6}$$

d_{Cu} is the grain size of the Cu phase, about 200 nm from Fig. 6c, and the σ_{GB} is calculated for 293 MPa, at a drawn strain $\epsilon = 3.94$. The σ_{DIS} can be calculated by:

$$\sigma_{DIS} = \alpha MGb\sqrt{\rho} \tag{7}$$

In which, α is a constant and taken as 0.24 for FCC metals; M is the Taylor factor of 3.06; G stands for the shear modulus, for Cu it should be 45.6 GPa; b represents the Burgers vector, the value is calculated by $\frac{\sqrt{2}}{2}a = 0.256\,nm$, a is the lattice constant; ρ is measured by XRD on behalf of the dislocation density, about $2.2 \times 10^{14}/\text{m}^2$. It should be noted that the dislocation density of Cu-phase in cold deformed Cu–Fe alloy is much smaller than that of the pure heavily deformed Cu. For example, the dislocation density in Cu-phase in a cold rolled Cu–10%Fe alloy plates is $1.2\times10^{14}/\text{m}^2$ while the drawn pure Cu wires are provided with a dislocation density of $5–7\times10^{14}/\text{m}^2$ [7,19]. As discussed above, the DRR of Cu-phase during the drawing is responsible for the low-density dislocation. Hence, the value of σ_{DIS} is calculated as 127 MPa. In addition, the contribution of the Fe-precipitation to the strength of Cu-phase should be considered. In this study, it is found that small Fe particles in Cu-phase maintain almost a spherical shape after drawing deformation. It seems that the hard iron particles didn't deform in the Cu matrix and play as a barrier for the plastic deformation of the Cu phase. As shown in Fig. 12a, the spherical nano iron Fe particles divide the surrounding copper matrix into four sub-structures. This is quite different from the precipitation hardening where the matrix has a high density of nano-precipitates and very few dislocation boundaries. Thus, the separate strengthening contribution from Fe particles is assumed negligible. The strengthening of Fe iron particles in Cu could be merged into grain refinement. Hence, the σ_{yCu} is estimated to be 420 MPa for the presented Cu–Fe wire at $\varepsilon = 3.94$.

According to the report of Feng et al. [20], the strength of Fe phase based on dislocation and boundary strengthening can be comprehensively calculated using Formula (8) as follows:

$$\sigma_{yFe} = 62 + 5.9Gb \times d_{Fe}^{-1} \tag{8}$$

where 62 (MPa) is the fraction stress, calculated from the fully recrystallized Fe wire.; G represents the shear modulus, approximately 81.7 GPa; b stands for the Burgers vector, 0.248 nm; and d_{Fe} is the average lamellar spacing for Fe, which was measured from the HRTEM to be 54 nm (Fig. 5e). The nano-lamellar structure of the Fe-phase is also separated by thin Cu nano-lamellae. The nano-lamellae Cu can hinder dislocation slip, and large numbers of dislocations were pinned by the phase boundary, as indicated by the white arrow as shown in Fig. 12b. The average free path of dislocation motion will be reduced by thinning the lamella, and the strengthening effect of the wire is more effective. Therefore, the strengthening from the Cu/Fe nano lamellae are assumed as boundary strengthening. According to the formula mentioned above, the calculated σ_{yFe} is 2275 MPa. Based on Formula (4), the σ_y is estimated to be 828 MPa. Taking into account the measurement error of the fiber thickness, it is considered that the predicted value is in good agreement with the measured yield strength of 824 MPa.

Above all, it can be found that the strength of the drawn Cu-20% Fe wire is mainly related to the grain refinement. It should be pointed out that the ROM law was considered not suitable for calculating the yield strength of drawn Cu–Fe alloy wires in previous studies [18]. Since the Cu particles in the Fe phase are continuously elongated during the drawing process, the refinement of the Fe phase is more obvious than that of pure iron wire drawing. In this work, we chose to use formula (8) instead of formula (1) to calculate the strength of the Fe phase, and the results show that the ROM method is still applicable to predicate the strength of drawing Cu–Fe wires.

4.3. Electrical conductivity

The electrical conductivity is not only affected by environmental factors and the intrinsic properties of materials but also related to changes in microstructure, including dislocations, grain boundaries (GBs), precipitated phases and solute atoms. Matthiessen et al. [37]. described this behavior as follows:

$$\Omega_i = \Omega_d + \Omega_b + \Omega_s + \Omega_p \tag{9}$$

where Ω_i represents the increment in the metal resistivity due to impurities and defects, Ω_d-dislocation scattering resistivity, Ω_b-interface scattering resistivity, Ω_s-solute scattering resistivity, and Ω_p-precipitate strain field scattering resistivity. For the Cu-20% Fe alloy, the resistivity of copper is much lower than that of iron, so the change in EC is mainly

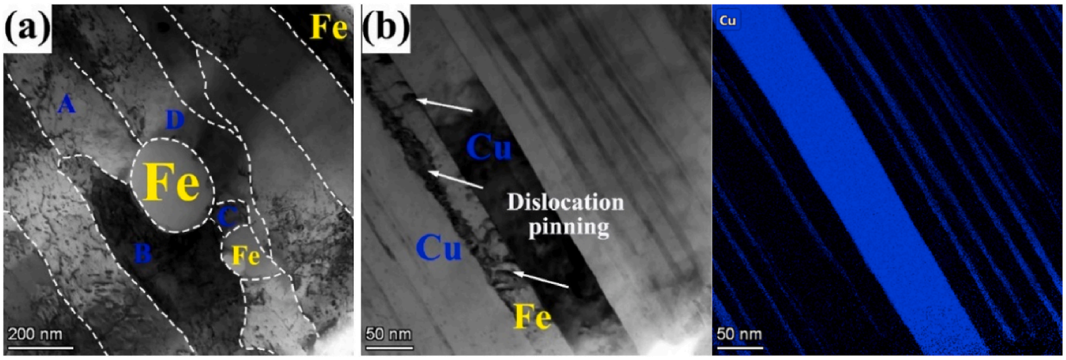

Fig. 12. Wire with ε = 3.94 (a) spherical Fe nanoparticles, (b) lamellar Fe fibers.

related to the deformation structure of copper. The resistivity of dislocation could be evaluated as [19]:

$$\Omega_d = \rho\cdot\Delta\Omega_d \tag{10}$$

Where, ρ is the dislocation density in copper phase, and $\Delta\Omega_d$ is the dislocation electrical resistivity of Cu, as reported by $2\times 10^{-25}\Omega\cdot m^3$. In cold drawn Cu–Fe wires, the ρ was measured to $2.2\times10^{14}/\mathrm{m}^2$. Then the maximum value of Ω_d was estimated about $0.004\times10^{-8}\ \Omega\cdot m$. Compared with the intrinsic resistivity of copper $1.724\times10^{-8}\ \Omega\cdot m$, the increased resistivity of dislocation is almost negligible. And grain boundary resistivity could be expressed as [38]:

$$\Omega_b = \frac{2}{3}\Delta\Omega_{gb}\left(\frac{S}{V}\right) \tag{11}$$

Where, $\Delta\Omega_{gb}$ is the grain boundary electrical resistivity of Cu, is $2.04\times 10^{-16}\Omega\cdot m^2$; $\frac{S}{V}$ is the GB area per volume, for tetra-kaidecahedral grains usually taken as 2.37/d. Meanwhile, the Cu grains were seriously elongated along the drawing direction (as shown in Fig. 6). Therefore, the GB of Cu can be separated as the GB parallel to the axial direction (GBp) and the GB vertical to the axial direction (GBv), respectively. Electrons are transmitted along the axial direction in the wire, so the electron scattering induced by GBv should be much greater than that induced by GBp. Compared with the equiaxed structure, the elongated grains are more conducive to the transport of electrons. However, the values of resistivity induced by GBv and GBp cannot be acquired, then the resistivity of elongated grains cannot be evaluated accurately. Wei et al. [39]. calculated the influence of defects on EC in. The results show that the effect of grain boundaries on electron scattering is far greater than that of dislocations and vacancies, but only accounts for 25% of the total increased resistivity. The resistivity increased by solid solution was analyzed, and Ω_s can be calculated by Nordheim-rule [16]:

$$\Omega_s = A\cdot C\cdot(1 - D\cdot C) \tag{12}$$

Where, A and D is empirical constant and C is solute con-centration in the matrix. Although the mutual solubility of copper and iron at room temperature is very low, and annealing treatment promote the further precipitation of the second phase, a small amount of solid solution elements will inevitably remain in the matrix. According to the result, the interplanar spacing of $(111)_{\mathrm{Cu}}$ is about 2.0865 Å, slightly larger than the standard value of 2.086 Å. In annealed Cu–Fe alloy, the increase in interplanar spacing of Cu is caused by the lattice expansion induced by the solid solution of Fe. As shown in Fig. 13, the peak positions of the copper phase and iron phase do not change for a strain of lower than 2.06. When the strain increased to 3.94, the copper (111) peak shift to the left, the lattice constants of the copper phase is increased, indicating that more iron element dissolved into Cu matrix. Quelennec [40] also report that the iron phase can be dissolved after high-pressure torsion to form a supersaturated solid solution in the copper matrix. The content of solid solution iron in the copper matrix can reach as high as 12 at%, much higher than the solid solubility of iron in copper under equilibrium conditions.

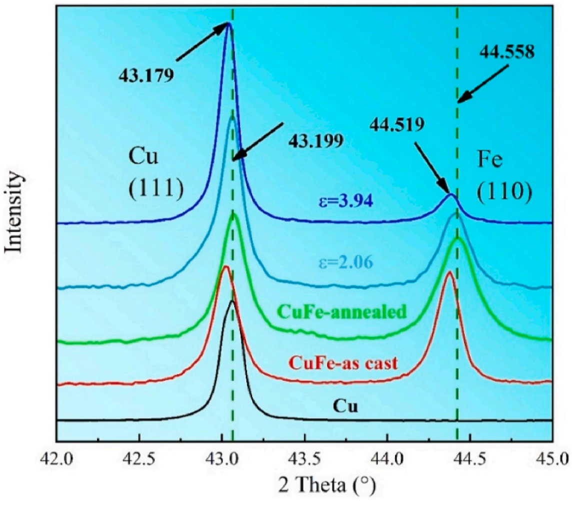

Fig. 13. XRD for Cu–20%Fe with θ from 42° to 45°.

The relationship between electrical resistivity and average radius of precipitates is established by Gibbs Thomson equation [41]:

$$\Omega_p = \Delta\Omega_P\cdot exp\left(\frac{2\cdot\gamma\cdot V_m}{R_c\cdot T\cdot r}\right) \tag{13}$$

Where, $\Delta\Omega_P$ is the electrical resistivity coefficient of the precipitated phase; γ is the surface energy; V_m is the molar volume; R_c is the molar gas constant; T is the temperature and r is the diameter of the precipitated particles. In formula (13), factors other than r can be considered as constants. Therefore, it can be considered that the resistivity caused by precipitation decreases with the increase of particle size. Although there is a small amount of iron precipitates in the copper matrix, these precipitates are hardly affected by the drawing deformation (shown in Fig. 12a), and drawing will not induce new particle precipitation. Therefore, it can be considered that the resistivity caused by precipitation remains almost unchanged in the drawing process. However, the fragmentation of iron fibers will also produce a large number of fine second phases, resulting in additional electron scattering. It can be seen from Fig. 4 that, when $\epsilon \geq 2.06$, the Fe phase has been almost parallel to the drawing direction. With the continuous increase of drawing strain, the Fe lamellar is not only continuously refined, but also a lot of fragmentation. The fragmentation of Fe fiber will greatly increase the interface density between Fe and Cu, and have a serious scattering effect on electronic transmission. The effect of the phase boundary on the EC is similarly described in the report of Zou et al. [17,18].

Fig. 7b shows that the change in EC can be divided into four stages with the increasing number of drawing passes: In 1st stage, deformation produces a large number of crystal defects and sub-crystals, resulting in an increase in resistivity. In 2nd stage, the EC is increased significantly. DRR reduces defects in the structure, and the copper grains and Fe phase are elongated along the drawing direction, the resistivity caused by the grain boundaries and phase boundary is reduced. In 3rd stage, the EC is stable between strains of 1.16–2.06. At this stage, while the grains are elongated to decrease the resistivity, and a large number of sub-grains are formed in the Cu grains to increase the resistivity. Thus, an EC balance is reached between DRR and plastic deformation. In 4th stage, when the drawing strain is greater than 2.06, the EC continues to decline. It is because that due to severe drawing deformation, the Fe fiber is broken and partially dissolved, resulting in additional resistivity due to the new phase boundary and solid solution. Besides, DRR is inhibited due to the solid solution of iron and faster heat dissipation of filaments, more small-angle misorientation is produced in the structure with a drawn strain of 3.94, as shown in Fig. 11. Based on the above analysis, it can be concluded that when $\epsilon < 2.06$, the EC of drawn Cu–Fe wires is mostly affected by the morphology of copper grain; When $\epsilon > 2.06$, the EC is dominated affected by the strain-induced solid solution of Fe element and the fragmentation of Fe fibers.

Apart from that, the lattice constant change obtained by the XRD, HRTEM also shows interesting result. Fig. 14a shows a fiber structure between Cu and Fe phase, and Fig. 14b is a local magnification diagram of the red frame in Fig. 14a. The structure of phase boundary is seriously distorted. Similar structures are also observed in heavily strained Cu–Nb and Cu–Nb–Ag alloy, and are proposed to be a mechanical alloying and amorphization [42,43]. Therefore, in 4th stage, the mechanical alloying and amorphization of Fe in Cu-phase is believed to decrease the EC of the alloy wire. But for the nano lamellar of Cu in the Fe phase, a relatively complete coherent relationship remains after large strain drawing

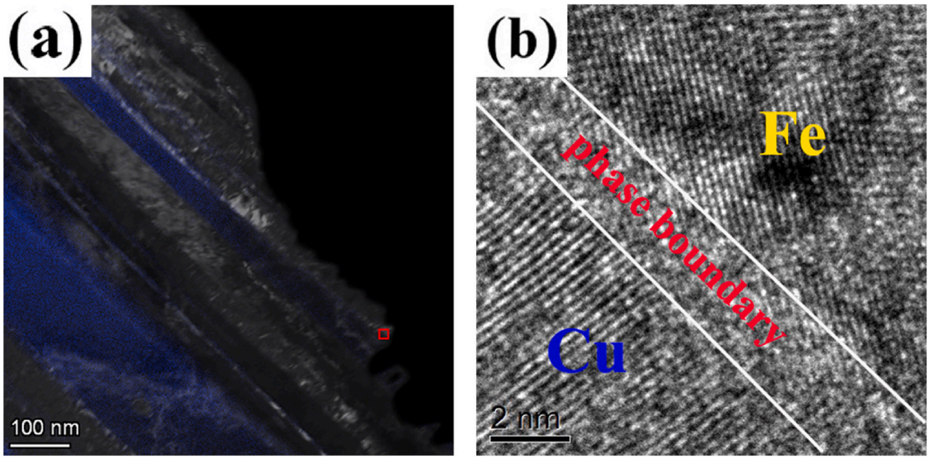

Fig. 14. (a) Fiber structure of Cu and Fe phase (blue area is the distribution of Cu elements); (b) the FFT of red frame. (For interpretation of the references to colour in this figure legend, the reader is referred to the Web version of this article.)

deformation, as shown in Fig. 15 (yellow represents Fe and blue is Cu). Arising from the excellent plastic deformation ability of Cu, makes it easier to produce coordinated deformation with the Fe phase, so the coherent relationship is maintained. It is worth noting that, the deformation of Fe phase is greatly affected by size. The micron Fe phase is seriously elongated in the extension drawing direction, while the nano Fe particles are hardly deformed. Besides, the coordination deformation of the Fe particles in the Cu matrix is completely different from that Cu particles in Fe phase. For example, the Cu particles in the Fe phase show better coordinated deformation, while the deformation of Fe particles in the Cu matrix is relatively difficult. The uncoordinated deformation of the two phases may produce higher insulating heat, and lead to the

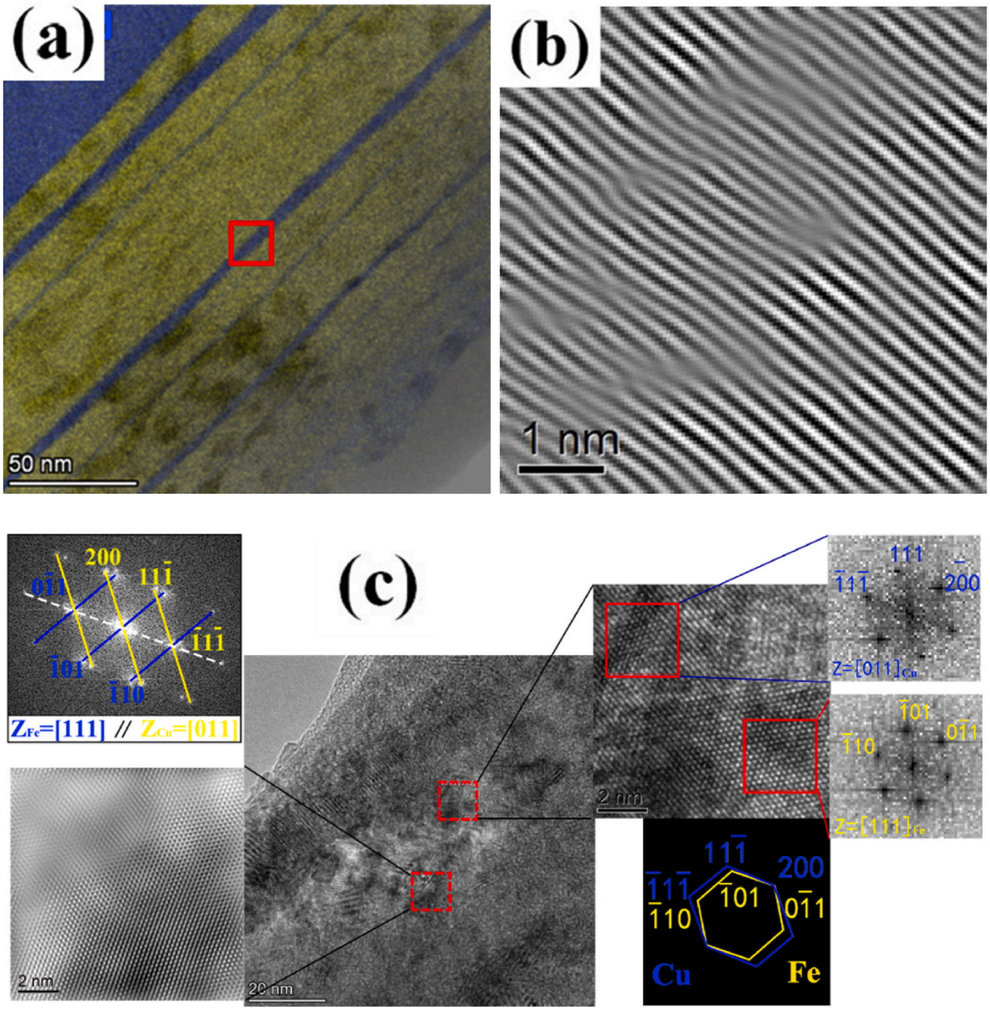

Fig. 15. Coherent relationship between Fe phase and the inside Cu fiber.

drawing structure to be completely different from that of the single phase.

Above all, to obtain higher strength while minimizing the reduction of electrical conductivity. It is necessary to promote the fibrillation and ultra-fineness of the Fe phase, and avoiding the fragmentation of Fe fibers caused by severe drawing deformation. Then we propose a new design strategy: Firstly, select appropriate drawing deformation Cu–Fe alloy wire (the Fe fiber is not seriously broken); Then, the selected Cu–Fe alloy wire is subject to intermediate annealing, to promote the precipitation of Fe element from Cu matrix, and the annealing temperature should not be too high to avoid the spheroidization of Fe fiber; Finally, the annealed wires will be continue cold drawn at room temperature. It is predicted to form a Cu/Fe nano-lamellar structure, which both beneficial to strength and electrical conductivity. Relevant research deserves our continuous attention in the future.

5. Conclusions

High properties Cu80–Fe20 alloy wires are prepared by a process combining hot-forged, pre-drawing annealing and cold drawing. The main conclusion could be concluded:

1) After pre-drawing annealing, both the Cu particles in Fe-phase and Fe-particles in Cu-phase share a K–S orientation relationship with its matrix, that is $(1\bar{1}1)_{Cu}//(\bar{1}10)_{Fe}$, $<011>_{Cu}//<111>_{Fe}$.
2) As the drawing strain increased to 3.94, the Cu phase is slightly elongated along the drawing direction, and the nano Fe particles in the Cu phase are less affected by drawing. The Fe phase and nano Cu particles inside form a nano-lamellar structure along the drawing direction.
3) The strength of Cu–Fe alloy is greatly affected by Fe lamellar spacing. The refinement of Fe phase is more obvious due to the existence of nano Cu fiber. The wire at a strain of 3.94, with an average boundary spacing of 54 nm, had a tensile strength of 863 MPa and electrical conductivity of 47 %IACS.
4) At low drawing strain, the EC is greatly affected by grain morphology and dynamic recrystallization. When the drawing strain is greater than 2, the decrease in electrical conductivity is related to the fragmentation of Fe fibers to increase the phase boundary and the partial dissolution of Fe particles.

Data availability statement

All data included in this study are available upon request contact with the corresponding authors.

CRediT authorship contribution statement

Fei Yang: Writing – review & editing, Executor of the experiment; Writing and Editing. **Liming Dong:** Writing – review & editing, Executor of the experiment; Writing and Editing. **Lichu Zhou:** Formal analysis, Analysis of research results. **Ning Zhang:** Investigation, Investigation of microstructure. **Xuefeng Zhou:** Formal analysis, Analysis of research results. **Xiaodan Zhang:** Writing – review & editing, Reviewing and Editing. **Feng Fang:** Writing – review & editing, Supervision, Designer of the experiment; Editing.

Declaration of competing interest

The authors declare that they have no known competing financial interests or personal relationships that could have appeared to influence the work reported in this paper.

Acknowledgment

This work was supported by National Natural Science Foundation of China (No. 52171110) and the research fund of Jiangsu Key Laboratory of Advanced Metallic Materials, P.R. China (No. AMM2020A02), and was also supported by the computational resources from the Big Data Center of Southeast University. F. Yang acknowledges the support provided by China Scholarship Council [2021]-70. X. Zhang and L. Zhou acknowledge the support by a research grant (00028216) from VILLUM FONDEN.

References

[1] D.W. Yuan, H. Zeng, X.P. Xiao, H. Wang, B.J. Han, B.X. Liu, B. Yang, Effect of Mg addition on Fe phase morphology, distribution and aging kinetics of Cu-6.5Fe alloy, Mater. Sci. Eng. 812 (2021), 141064.

[2] M. Wang, Q.R. Yang, Y.B. Jiang, Z. Li, Z. Xiao, S. Gong, Y.R. Wang, C.L. Guo, H. G. Wei, Effects of Fe content on microstructure and properties of Cu–Fe alloy, Trans Nonferrous Met Soc. China. 31 (2021) 3039–3049.

[3] S.C. Liu, J.C. Jie, Z.K. Guo, G.M. Yin, T.M. Wang, T.J. Li, Solidification microstructure evolution and its corresponding mechanism of metastable immiscible Cu80Fe20 alloy with different cooling conditions, J. Alloys Compd. 742 (2018) 99–106.

[4] F. Wang, K. Wakoh, Y. Li, S. Ito, K. Yamanaka, Y. Koizumi, A. Chiba, Study of microstructure evolution and properties of Cu-Fe microcomposites produced by a pre-alloyed powder method, Mater. Des. 126 (2017) 64–72.

[5] Y. Pang, G. Chao, T. Luan, S. Gong, Y. Wang, Z. Jiang, Z. Xiao, Y. Jiang, Z. Li, Microstructure and properties of high strength, high conductivity and magnetic Cu–10Fe-0.4Si alloy, Mater. Sci. Eng. 826 (2021), 142012.

[6] N.D. Stepanov, A.V. Kuznetsov, G.A. Salishchev, N.E. Khlebova, V.I. Pantsyrny, Evolution of microstructure and mechanical properties in Cu–14%Fe alloy during severe cold rolling, Mater. Sci. Eng. 564 (2013) 264–272.

[7] M. Wang, Y.B. Jiang, Z. Li, Z. Xiao, S. Gong, W.T. Qiu, Q. Lei, Microstructure evolution and deformation behaviour of Cu-10 wt%Fe alloy during cold rolling, Mater. Sci. Eng. 801 (2021), 140379.

[8] D. Yuan, X. Xiao, X. Luo, H. Wang, B. Han, B. Liu, B. Yang, Effect of multi-stage thermomechanical treatment on Fe phase evolution and properties of Cu-6.5Fe-0.3Mg alloy, Mater. Char. 185 (2022), 111707.

[9] P. Zhang, X. Yuan, Y. Li, Y. Zhou, R. Lai, Y. Li, Q. Lei, A. Chiba, Influence of minor Ag addition on the microstructure and properties of powder metallurgy Cu-10 wt% Fe alloy, J. Alloys Compd. 904 (2022), 163983.

[10] J.D. Verhoeven, S.C. Chueh, E.D. Gibson, Strength and conductivity ofin situ Cu-Fe alloys, J. Mater. Sci. 24 (1989) 1748–1752.

[11] A. Chatterjee, E. Sprague, J. Mazumder, A. Misra, Hierarchical microstructures and deformation behavior of laser direct-metal-deposited Cu–Fe alloys, Mater. Sci. Eng. 802 (2021), 140659.

[12] X.P. Lu, D.W. Yao, Y. Chen, L.T. Wang, A.P. Dong, L. Meng, J.B. Liu, Microstructure and hardness of Cu-12% Fe composite at different drawing strains, J. Zhejiang Univ. - Sci. 15 (2014) 149–156.

[13] P. Zhang, Q. Lei, X.B. Yuan, X. Sheng, D. Jiang, Y.P. Li, Z. Li, Microstructure and mechanical properties of a Cu-Fe-Nb alloy with a high product of the strength times the elongation, Mater. Today Commun. 25 (2020), 101353.

[14] J.M. Guo, M.J. Duarte, Y. Zhang, A. Bachmaier, C. Gammer, G. Dehm, R. Pippan, Z. Zhang, Oxygen-mediated deformation and grain refinement in Cu-Fe nanocrystalline alloys, Acta Mater. 166 (2019) 281–293.

[15] W.A. Spitzig, Strengthening in heavily deformation processed Cu-20% Nb, Acta Metall. Mater. 39 (1991) 1085–1090.

[16] J.P. Hou, R. Li, Q. Wang, H.Y. Yu, Z.J. Zhang, Q.Y. Chen, H. Ma, X.M. Wu, X.W. Li, Z.F. Zhang, Three principles for preparing Al wire with high strength and high electrical conductivity, J. Mater. Sci. Technol. 35 (2019) 742–751.

[17] M. Wang, R. Zhang, Z. Xiao, S. Gong, Y.B. Jiang, Z. Li, Microstructure and properties of Cu-10 wt%Fe alloy produced by double melt mixed casting and multi-stage thermomechanical treatment, J. Alloys Compd. 820 (2020), 153323.

[18] J. Zou, D.P. Lu, Q.F. Fu, K.M. Liu, J. Jiang, Microstructure and properties of Cu–Fe deformation processed in-situ composite, Vacuum 167 (2019) 54–58.

[19] F. Yang, L. Dong, L. Cai, L. Wang, Z. Xie, F. Fang, Effect of cold drawing strain on the microstructure, mechanical properties and electrical conductivity of low-oxygen copper wires, Mater. Sci. Eng. 818 (2021), 141348.

[20] H.C. Feng, F. Fang, X.F. Zhou, X.D. Zhang, Z.H. Xie, J.Q. Jiang, Heavily cold drawn iron wires: role of nano-lamellae in enhancing the tensile strength, Mater. Sci. Eng. 796 (2020), 140017.

[21] K.M. Liu, D.P. Lu, H.T. Zhou, Z.B. Chen, A. Atrens, L. Lu, Influence of a high magnetic field on the microstructure and properties of a Cu–Fe–Ag in situ composite, Mater. Sci. Eng. 584 (2013) 114–120.

[22] Z. Xie, H. Gao, J. Wang, B. Sun, Effect of homogenization treatment on microstructure and properties for Cu–Fe–Ag in situ composites, Mater. Sci. Eng. 529 (2011) 388–392.

[23] Z.W. Wu, J.D. Zhang, Y. Chen, L. Meng, Effect of rare earth addition on microstructural,mechanical and electrical characteristics of Cu-6% Fe microcomposites, J. Rare Earths 27 (2009) 87–91.

[24] Y. Li, D.N.Q. Yi, J.B. Zhang, Comparative study of the influence of Ag on the microstructure and mechanical properties of Cu-10Fe in situ composites, J. Alloys Compd. 647 (2015) 413–418.

[25] Q.Z. Mao, L. Wang, J.F. Nie, Y.H. Zhao, Enhancing strength and electrical conductivity of Cu–Cr composite wire by two-stage rotary swaging and aging treatments, Composites Part B 231 (2022), 109567.

[26] Z. Lai, Y. Mai, H. Song, J. Mai, X. Jie, Heterogeneous microstructure enables a synergy of strength, ductility and electrical conductivity in copper alloys, J. Alloys Compd. 902 (2022), 163646.

[27] G.Y. Li, S.Y. Li, L. Li, D.T. Zhang, Y.X. Tong, A high strength and high electrical conductivity CuCrZr alloy prepared by aging and subsequent cryorolling, Vacuum 190 (2021), 110315.

[28] S.Z. Han, J. Lee, S.H. Lim, J.H. Ahn, S. Kim, Optimization of conductivity and strength in Cu-Ni-Si alloys by suppressing discontinuous precipitation, Met. Mater. Int. 22 (2016) 1049–1054.

[29] Y. Li, Z. Xiao, Z. Li, Z. Zhou, Z. Yang, Q. Lei, Microstructure and properties of a novel Cu-Mg-Ca alloy with high strength and high electrical conductivity, J. Alloys Compd. 723 (2017) 1162–1170.

[30] B.B. Zhang, N.R. Tao, K. Lu, A high strength and high electrical conductivity bulk Cu-Ag alloy strengthened with nanotwins, Scripta Mater. 129 (2017) 39–43.

[31] C. Ding, J. Xu, D. Shan, B. Guo, T.G. Langdon, Sustainable fabrication of Cu/Nb composites with continuous laminated structure to achieve ultrahigh strength and excellent electrical conductivity, Composites Part B 211 (2021), 108662.

[32] S. Lee, Y.D. Im, R. Matsumoto, H. Utsunomiya, Strength and electrical conductivity of Cu-Al alloy sheets by cryogenic high-speed rolling, Mater. Sci. Eng. 799 (2020), 139815.

[33] J.P. Hou, R. Li, Q. Wang, H.Y. Yu, Z.J. Zhang, Q.Y. Chen, H. Ma, X.M. Wu, X.W. Li, Z.F. Zhang, Breaking the trade-off relation of strength and electrical conductivity in pure Al wire by controlling texture and grain boundary, J. Alloys Compd. 769 (2018) 96–109.

[34] T. Baudin, A.L. Etter, R. Penelle, Annealing twin formation and recrystallization study of cold-drawn copper wires from EBSD measurements, Mater. Char. 58 (2007) 947–952.

[35] Y. Jiang, R.G. Gu, Y. Zhang, J.T. Hwang, Heterogeneous structure controlled by shear bands in partially recrystallized nano-laminated copper, Mater. Sci. Eng. 721 (2018) 226–233.

[36] F. Yang, L.M. Dong, X.J. Hu, X.F. Zhou, F. Fang, Effect of solution treatment temperature upon the microstructure and mechanical properties of hot rolled Inconel 625 alloy, J. Mater. Sci. 55 (2020) 1–14.

[37] P.V. Andrews, M.B. West, C.R. Robeson, The effect of grain boundaries on the electrical resistivity of polycrystalline copper and aluminium, Philos. Mag. A 19 (1969) 887–898.

[38] L. Qian, Electrical resistivity of fully-relaxed grain boundaries in nanocrystalline Cu, Scripta Mater. 50 (2004) 1407–1411.

[39] W. Zeng, J.W. Xie, D.S. Zhou, Z.Q. Fu, D.L. Zhang, E.J. Lavernia, Bulk Cu-NbC nanocomposites with high strength and high electrical conductivity, J. Alloys Compd. 745 (2018) 55–62.

[40] X. Quelennec, A. Menand, J.M. Le Breton, R. Pippan, X. Sauvage, Homogeneous Cu–Fe supersaturated solid solutions prepared by severe plastic deformation, Philos. Mag. A 90 (2010) 1179–1195.

[41] J.P. Hou, Q. Wang, Z.J. Zhang, Y.Z. Tian, X.M. Wu, H.J. Yang, X.W. Li, Z.F. Zhang, Nano-scale precipitates: the key to high strength and high conductivity in Al alloy wire, Mater. Des. 132 (2017) 148–157.

[42] D. Raabe, S. Ohsaki, K. Hono, Mechanical alloying and amorphization in Cu–Nb–Ag in situ composite wires studied by transmission electron microscopy and atom probe tomography, Acta Mater. 57 (2009) 5254–5263.

[43] M. Demkowicz, R. Hoagland, J. Hirth, Interface structure and radiation damage resistance in Cu-Nb multilayer nanocomposites, Phys. Rev. Lett. 100 (2008), 136102.